www.sciencemag.org/cgi/content/full/1149926/DC1

# Supporting Online Material for

## Million-Degree Plasma Pervading the Extended Orion Nebula

Manuel Güdel,* Kevin R. Briggs, Thierry Montmerle, Marc Audard, Luisa Rebull, and Stephen L. Skinner

*To whom correspondence should be addressed. E-mail: guedel@astro.phys.ethz.ch

Published 29 November 2007 on *Science* Express
DOI: 10.1126/science.1149926

**This PDF file includes:**

**Supporting Online Material**

**Materials and Methods**

## 1. Reduction of the XMM-Newton X-ray data

All X-ray data discussed here were taken with the European Photon Imaging Cameras (EPIC) on board the X-Ray Multi-Mirror Satellite XMM-Newton, with an angular resolution of 5 arcseconds and a field of view of 30 arcminutes each. One of these Charge Coupled Device (CCD) cameras is of the PN type *(14)* and two are of the MOS type *(15)*. The middle field in Fig. 2A was observed on 2005 February 18 for ≈22 ks and on 2006 March 2 for ≈91 ks, the upper left field on 2001 October 3 for ≈39 ks, and the lower left field on 2001 September 15 for ≈22 ks.

Our data reduction involved standard procedures in the XMM-Newton Science Analysis System (SAS) software. Imaging analysis was performed using SAS v6.1. Spectral analysis took advantage of the improved treatment of extended sources offered in SAS v7.0.

Photon event lists in each of the three EPIC cameras were produced using the SAS EPCHAIN and EMCHAIN tasks for the PN and MOS data, respectively. Filtering of these event lists and exclusion of time intervals affected by high background were conducted as described by Güdel et al. *(S1)*.

The three-color images in Fig. 2A were constructed using data from eight XMM-Newton observations of four different, overlapping fields. In each of three energy bands – 0.3-1.0 keV, 1.0-2.0 keV and 2.0-7.3 keV – images were extracted from the event list for each camera and observation and mosaicked using the EMOSAIC task. Each image mosaic was adaptively smoothed *(S2)* to achieve a desired signal-to-noise ratio of 5 using ASMOOTH. A mask was employed to define areas of active CCD to be smoothed. Exposure maps account for the different exposure times of the observations (from 20 to 91 ks) and the lower sensitivity of the MOS cameras compared to the PN. These were produced for each camera, observation and energy band using EEXPMAP, and the MOS exposure times were converted to PN-equivalent exposure times by dividing by a band dependent factor (4.0, 2.9 and 2.7 for the 0.3-1.0 keV, 1.0-2.0 keV and 2.0-7.3 keV bands, respectively, as appropriate for the typical X-ray spectrum of young stars) before a mosaic was made for each band. The mosaicked exposure map was scaled to have a peak value of 1 to maintain counts as the units of the images. The exposure maps do not account for the decreasing sensitivity away from the detector center (the so-called vignetting) as this would distractingly accentuate the background component in the outer region of each observed field, because this particle-induced background is not subject to vignetting. The brightness of off-axis sources therefore appears lower (by up to a factor 2.5 at the very edge of the field of view) with respect to on-axis sources. Three-color images were generated by the Chandra CIAO software package task DMIMG2JPG *(S3)*

using a square-root scaling and minimum and maximum pixel values of 0 and 5 in each energy band.

The X-ray image in Fig. 2B was produced using data from only the longest observation (67 ks useful PN exposure time; 91 ks MOS) of the field containing the diffuse soft X-ray emission. As described above, images in the 0.3-1.0 keV and 1.0-2.0 keV energy bands were smoothed using ASMOOTH, but this time a mask was employed that excluded regions around point sources from the smoothing and a signal-to-noise of 20 was desired, in order to show the diffuse emission. Point sources were detected and parameterized (actually in 0.5-2.0 keV, 2.0-7.3 keV and 0.5-7.3 keV images as part of a parallel investigation) using a combination of SAS tasks and FTOOLS described in Güdel et al. *(S1)*. Elliptical source exclusion regions were calculated using the REGION task (Fig. S1A). These defined the point spread function contour at which the surface brightness of counts from the source fell to 0.3 times that from the local background. These were made into a mask, using REGIONMASK, which was then combined with the mask defining the active CCD area.

The image in Fig. 2B shows the ratio of the 0.3-1.0 keV and 1.0-2.0 keV source-excluded smoothed images on a logarithmic intensity scale. This ratio is closely representative of the measured 0.3-1.0 keV flux because this excess emission is mostly seen in the softer band (Fig. S1B) while the harder band shows a nearly flat count distribution in the EON, dominated by background radiation (Fig. S1C). But the ratio image (Fig. 2B) has two key advantages over the 0.3-1.0 keV image alone (Fig. S2). Firstly, the soft-band image shows excess values not only where we see the soft diffuse emission in Fig. 2A but also around the confusion of sources close to Theta 1 Ori C. As the typical spectrum of the point sources (see e.g. Fig. 3) is harder than that of the diffuse emission (especially in this more heavily-absorbed region of the nebula), this excess, unlike that of the true soft diffuse emission, also shows up in the 1.0-2.0 keV image and is cancelled out in the ratio image. Secondly, the two single-band images each suffer from a similar amount of vignetting, so while the diffuse emission in the outer regions of the 0.3-1.0 keV image appears faint and is poorly seen, vignetting has a much smaller effect in the ratio image, enabling the diffuse emission close to the edge of the field of view to be much more clearly seen.

Somewhat coincidentally the typical value of the ratio in regions of normal background is approximately 1. The image in Fig. 2B shows a logarithmic scaling for the X-rays from 1.3 to 4, which shows the soft diffuse emission.

The extraction of X-ray spectra also used only this longest observation, and concentrated on data from the most sensitive EPIC instrument, the PN CCD camera. Polygonal extraction regions for the northern and southern areas of diffuse emission were defined by viewing the 0.3-1.0 keV image in the DS9 imaging software (Fig. S3). Regions around point sources were excluded as noted above. Nevertheless, due to the relatively large point-spread function of XMM-Newton and the detection of “out of time events” at

false positions along the readout direction while the CCD is being read out, a considerable number of counts from the point sources still contaminate the spectra of the diffuse emission. This contamination was modeled by extracting a composite spectrum of all point sources in each of the northern and southern extraction regions and simultaneously fitting the diffuse and point-source spectra (see below). Circular extraction regions with the small radius of 10 arcsec, which enclose approximately half of the total counts from each source, were used to minimize the contribution of diffuse emission to the point-source spectra.

A background spectrum was taken from a region where no soft diffuse emission was visible in a largely source-free area at the upper right of the detector (Fig. S3). As this region is further off-axis than the extraction regions for the diffuse emission and some components of the background are vignetted, the background was spectrum was scaled by factors 1.18 and 1.16 for the northern and southern diffuse regions, respectively. This scaling assigns all counts in the diffuse spectra in the 4-7 keV region to the background (i.e. it is the maximum possible correction), which is consistent with the expected vignetting in this energy range and off-axis angle *(S4)*. The background spectrum was scaled to the areas of the two diffuse-source areas and was then subtracted.

All PN spectra were extracted by selecting only CCD events with event patterns 0-4 (attributed to source X-rays rather than cosmic ray hits of the CCD) while MOS spectra required no further filtering.

The spectral response of the instrument was modeled for each spectrum by generating response matrices using the RMFGEN task and ancillary response files using ARFGEN, with the spatial variation over the extraction area modeled as a flat detector map with 20 x 20 pixels.

**2. Reduction of the Spitzer Space Telescope infrared data**

The Spitzer observations of the Orion nebula were obtained as part of guaranteed time observations (program 43, PI Fazio) in late 2004 and are described further in *(S5)*. Standard pipeline products processed by the Spitzer Science Center (SSC) are basic calibrated data (BCD) products which include flux-calibrated individual frames, errors, etc., and so-called "Post-BCD" (Post-basic calibrated data) products, which include mosaics of individual frames, mosaics of errors, etc. The pipeline has applied all of the standard corrections astronomers usually use when creating mosaics, for example, applying outlier rejection to remove the signatures of cosmic rays, and producing flux-calibrated images. We downloaded post-BCD from the Spitzer Science Center pipeline version 14.0. We used the SSC mosaicking and point-source extraction (MOPEX) software *(S6)* to combine the data into large images, separately for the different bands provided by the IRAC

instrument (3.6μm, 4.5μm, 5.8μm, and 8μm). The resultant integration time is 24 seconds per position and per channel.

**3. Spectral fits for the X-ray data**

The X-ray spectra were binned in energy, differently at different energies (in the 0.25-0.7 keV range: minimum of 30 counts per bin before background subtraction; in the 0.7-0.9 keV range: minimum of 100 counts for northern source and 500 counts for southern source; in the 0.9-1.38 keV and 1.58-4.0 keV ranges: minimum of 500 counts for the northern source, 2000 counts for the southern source; see Fig. 3). We have removed the bins around 1.5 keV due to strong contamination by an instrumental line of aluminum. The error bars attached to each data point reflect $1\sigma$ errors from counting statistics. The synthesized source spectra of the combined point sources were rebinned to a minimum number of 30 cts per bin.

Independent spectral fits showed that the diffuse emission originates from a dominant cool (1-2 MK) plasma but shows contributions from hotter plasma that are similar to the emission in the stellar point sources. As suggested above, this is expected because the extended instrumental wings of the point sources contaminate the diffuse areas. On the other hand, some diffuse emission is also included in the extracted stellar point-source spectra. We therefore modeled the spectra together, allowing for a variable contribution of the stellar emission to the spectra of the diffuse emission and vice versa, independently for the northern and southern areas.

Spectral fits were made in the XSPEC software *(S7)* using the APEC atomic emission line code for a hot, thermal plasma in collisional ionization equilibrium included in the software package. The diffuse emission was defined by one isothermal component (for each of the areas), while the stellar spectra required three isothermal components, each component described by its electron temperature and emission measure. An absorbing interstellar hydrogen column density, $N_H$, was simultaneously fitted, again independently for the diffuse emission and the point sources. Finally, we also considered element abundances. Most elements do not generate strong emission lines in our soft spectra of the diffuse emission. We therefore adopted their abundances as determined previously for the hot, X-ray emitting wind of $\theta^1$ Ori C *(S8)* with respect to the solar photospheric fraction *(S9),* namely Ne (1.04 times the solar fraction), Mg (0.94), Si (1.11), S (1.22), Ar (1.48), Ca (1.72), and Fe (0.62). We fitted C, N, and O abundances to the diffuse emission spectrum because these elements produce the dominant spectral contributions below 0.7 keV. For the stellar spectrum, we additionally fitted abundances of Ne, Mg, S, Si, Ar, and Fe that produce line emission features in the harder portion of the spectra. The remaining stellar element abundances were fixed at values commonly seen in young stellar X-ray sources *(S1)*. For the stellar spectra, we also held C and N fixed at such values because the dominant hot stellar plasma produces no discernible features of C and N at the soft end of the spectrum.

The results are given in Table S1. The errors give 1σ errors due to counting statistics and represent to the formal uncertainties of the parameters in the adopted, simplistic model. Unknown systematic uncertainties in the atomic emission line model and in the detector calibration would increase the error bars. The X-ray luminosity was determined by integrating the unabsorbed best-fit model spectrum over the energy range of 0.1-10 keV, assuming a distance of 400 pc *(S10-S12)*.

The stellar point-source spectra, not described in the Table, required three components with temperatures of 2.2 MK, 8.7 MK, and 27 MK with a ratio of emission measures of 1:3.4:9.4 for the northern area, and temperatures of 4.9 MK, 9.4 MK, and 30 MK with a ratio of emission measures of 1:1.4:3.1 for the southern area. The hottest components clearly dominate both stellar spectra, and the spectral flux is monotonically decreasing with decreasing photon energy below 1keV, the spectra thus showing a pronounced peak at 1 keV due to emission lines of iron and neon (Fig. 3). The stellar hydrogen absorption column densities amount to $1.1 \times 10^{21}$ $cm^{-2}$ and $8.5 \times 10^{20}$ $cm^{-2}$ for the N and S stellar sources, some of this material normally being confined to the immediate circumstellar environment. The coolest component of the stellar point source spectrum contributes ≈3% and ≈4% to the emission measure of the cool component collected from the diffuse areas. The three components of the scaled stellar point source spectrum together contribute only about 5% to the soft spectrum of the diffuse emission at 0.3-0.6 keV while they accurately explain all of the hard emission above 1 keV (Fig. 3), corroborating our view that the hard diffuse emission is due to contamination from stellar point sources.

Table S1 also lists some further parameters used in conjunction with the X-ray results to estimate physical source parameters. For these parameters (projected area, estimated volume, electron density, and plasma mass), we give values referring to a slab model (EON circular area with a radius of 2 pc and a depth of 0.9 pc, first number) and for a spherical model (a spherical volume filling the EON with a radius of 2 pc, second number).

**Supporting figures**

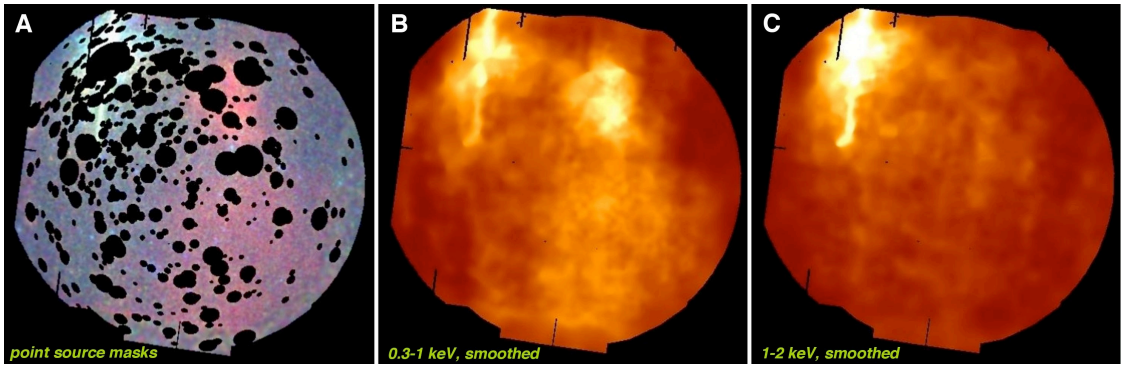


Figure S1: Left (A): X-ray image after excising the areas around the point sources. Middle (B) and Right (C): Smoothed X-ray images of the EON region. Both figures have been adaptively smoothed after removal of X-ray point sources. Panel (B) is for the 0.3-1.0 keV band, showing soft diffuse emission (in the right half) but also strong emission from the Trapezium cluster stars. Panel (C) shows the 1-2 keV band in which the Trapezium stars dominate.

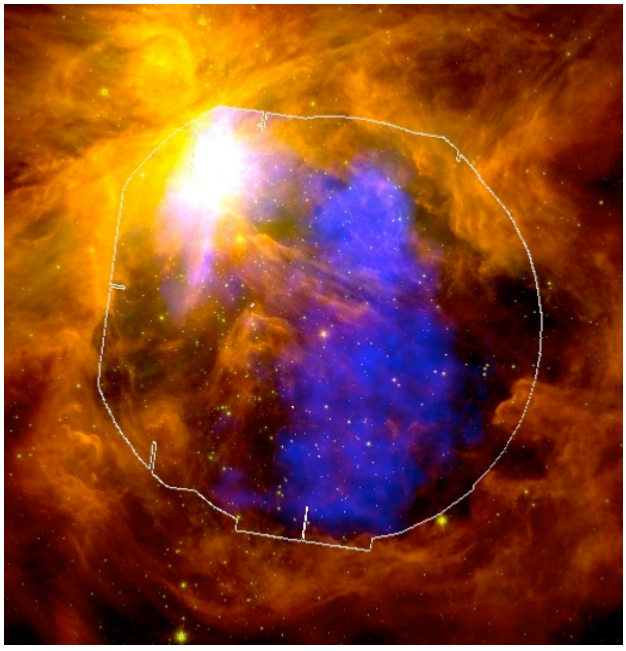

Figure S2: X-ray diffuse emission (blue) superimposed on a Spitzer composite image. This figure is analogous to Fig. 2B except that the flux in the 0.3-1 keV X-ray band is shown rather than its excess relative to the 1-2 keV band. The lack of vignetting correction suppresses X-rays near the border of the detector, and the broadband but predominantly harder X-rays from the Trapezium cluster saturate the upper left area.

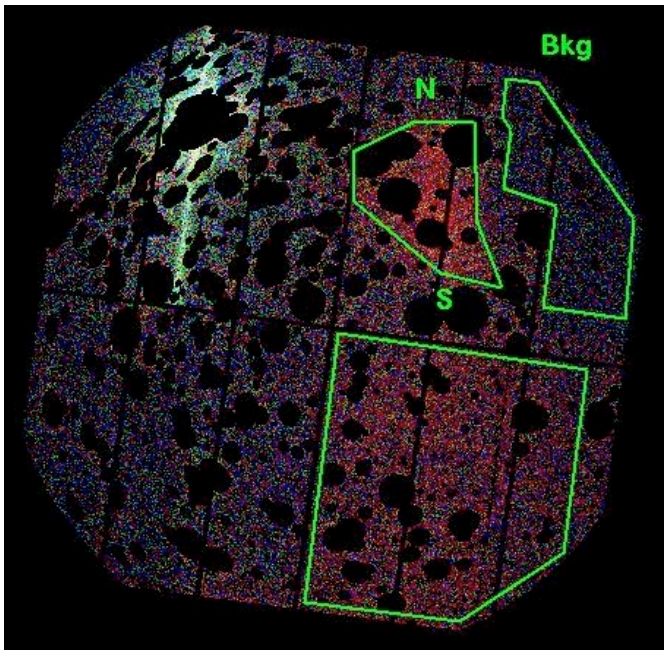


Figure S3: Extraction regions on the PN detector used for spectral analysis. The green polygons show the extraction regions for the northern diffuse source (upper left), the southern diffuse source (lower area), and the background area (upper right). The point sources have been removed, and the remaining counts on the detector have been color-coded as in Fig. 2A.

**Supporting table**

Table S1: Spectral interpretation and source geometry. The first seven parameters have been derived from fits of the observed X-ray spectra of diffuse emission with calculated model spectra of hot plasmas. The last four parameters are based on the observed and adopted geometric extent of the extended X-ray sources. Equal signs in the column for the southern area indicate identical values as for the northern area. Two numbers separated by a slash refer to two different geometric model assumptions (see text).

| *Parameter* | | *Unit* | *Northern Area* | *Southern Area* |
|---|---|---|---|---|
| Hydrogen column density | $N_H$ | $10^{20}$ cm$^{-2}$ | 4.1(±0.7) | 0.4(-0.4,+0.5) |
| Volume emission measure | EM | $10^{54}$ cm$^{-3}$ | 1.45(±0.25) | 1.88(±0.28) |
| Electron temperature | T | $10^6$ K | 1.73(±0.03) | 2.08(-0.02,+0.03) |
| Oxygen abundance | | - | 0.43(-0.04,+0.06) | = |
| Nitrogen abundance | | - | 1.5(-0.2,+0.3) | = |
| Carbon abundance | | - | 1.5(-0.2,+0.3) | = |
| X-ray luminosity | $L_X$ | $10^{31}$ erg s$^{-1}$ | 2.3 | 3.2 |
| Cross-sectional area | A | pc$^2$ | 0.24 | 1.38 |
| Volume | V | pc$^3$ | 0.22/0.97 | 1.24/5.5 |
| Electron density | $n_e$ | cm$^{-3}$ | 0.47/0.22 | 0.23/0.11 |
| Observed plasma mass | M | $M_\odot$ | 0.003/0.006 | 0.008/0.017 |

**Supporting References and Notes:**


S1. M. Güdel *et al.*, *Astron. Astrophys.* **368**, 353-377 (2007).
S2. H. Ebeling, D.A. White, F.V.N. Rangarajan, *Mon. Not. Royal Astron. Soc.* **368**, 65-73 (2006).
S3. A. Fruscione *et al.*, SPIE Proc. 6270, D.R. Silvia & R.E. Doxsey, Eds., 62701-12V (2006).
S4. J. Pradas, J. Kerp, *Astron. Astrophys.* **443**, 721-733 (2005).
S5. S.T. Megeath *et al.*, in *Massive Star Birth: A Crossroads of Astrophysics*, IAU Symposium Vol. 227, R. Cesaroni *et al.,* Eds. (Cambridge: Cambridge University Press, 2005) pp. 383-388.
S6. D. Makovoz, F.R. Marleau, *Publ. Astron. Soc. Pacific* **117**, 1113-1128 (2005).
S7. K. A. Arnaud, in *Astronomical Data Analysis Software and Systems V,* G. H. Jacoby, J. Barnes, Eds. (San Francisco, Astronomical Society of the Pacific, 1996), pp. 17-20.
S8. M. R. Gagné *et al., Astrophys. J.* **628**, 986-1005 (2005).
S9. E. Anders, N. Grevesse, *Geochim. Cosmochim. Acta* **53**, 197-214 (1989).
S10. R.D. Jeffries, *Mon. Not. Royal Astron. Soc.* **376**, 1109-1119 (2007).

S11. K.M. Sandstrom, J.E.G. Peek, G.C. Bower, A.D. Bolatto, R.L. Plambeck, *Astrophys. J.* **667**, 161-1169 (2007).
S12. K.M. Menten, M.J. Reid, J. Forbrich, A. Brunthaler, *Astron. Astrophys.* **474**, 515-520 (2007),